The atomic hydrogen content of galaxies as a function of group-centric radius

8 authors, including:

Wenkai Hu
Aix-Marseille Université
9 PUBLICATIONS   **97** CITATIONS

SEE PROFILE

Claudia Del P. Lagos
International Centre for Radio Astronomy Research
322 PUBLICATIONS   **8,396** CITATIONS

SEE PROFILE

Some of the authors of this publication are also working on these related projects:

EAGLE simulations View project

Early-type galaxies in GALFORM View project

The atomic hydrogen content of galaxies as a function of group-centric radius

Wenkai Hu [1,2,3,4]★ Luca Cortese [1,3]★ Lister Staveley-Smith [1,3]★ Barbara Catinella [1,3]
Garima Chauhan [1,3] Claudia del P. Lagos [1,3] Tom Oosterloo[5,6] and Xuelei Chen[4,7,8]

[1]*International Centre for Radio Astronomy Research (ICRAR), M468, University of Western Australia, 35 Stirling Hwy, WA 6009, Australia*
[2]*Aix Marseille Université, CNRS, LAM (Laboratoire d'Astrophysique de Marseille), F-13388 Marseille, France*
[3]*ARC Centre of Excellence for All Sky Astrophysics in 3 Dimensions (ASTRO 3D), Australia*
[4]*National Astronomical Observatories, Chinese Academy of Sciences, 20A, Datun Road, Chaoyang District, Beijing 100101, China*
[5]*ASTRON, the Netherlands Institute for Radio Astronomy, Postbus 2, NL-7990 AA Dwingeloo, the Netherlands*
[6]*Kapteyn Astronomical Institute, University of Groningen, PO Box 800, NL-9700 AV Groningen, the Netherlands*
[7]*Center of High Energy Physics, Peking University, Beijing 100871, China*
[8]*School of Astronomy and Space Science, University of Chinese Academy of Sciences, Beijing 100049, China*

ABSTRACT

We apply a spectral stacking technique to Westerbork Synthesis Radio Telescope observations to measure the neutral atomic hydrogen content (H I) of nearby galaxies in and around galaxy groups at $z < 0.11$. Our sample includes 577 optically selected galaxies (120 isolated galaxies and 457 satellites) covering stellar masses between 10^{10} and $10^{11.5}$ $M_\odot$, cross-matched with Yang's group catalogue, with angular and redshift positions from the Sloan Digital Sky Survey. We find that the satellites in the centres of groups have lower H I masses at fixed stellar mass and morphology (characterized by the inverse concentration index) relative to those at larger radii. These trends persist for satellites in both high-mass ($M_{halo} > 10^{13.5}$ h^{-1} $M_\odot$) and low-mass ($M_{halo} \leqslant 10^{13.5}$ h^{-1} $M_\odot$) groups, but disappear if we only consider group members in low local density ($\Sigma < 5$ gal Mpc^{-2}) environments. Similar trends are found for the specific star formation rate. Interestingly, we find that the radial trends of decreasing H I mass with decreasing group-centric radius extend beyond the group virial radius, as isolated galaxies close to larger groups lack H I compared with those located more than ~ 3.0 R_{180} away from the centre of their nearest group. We also measure these trends in the late-type subsample and obtain similar results. Our results suggest that the H I reservoir of galaxies can be affected before galaxies become group satellites, indicating the existence of pre-processing in the infalling isolated galaxies.

Key words: galaxies: evolution – galaxies: ISM – radio lines: galaxies.

1 INTRODUCTION

It is widely accepted that the evolution of a galaxy is significantly influenced by its environment (Dressler 1984; Blanton & Moustakas 2009; Benson 2010). Galaxies can be depleted in H I by (i) directly removing the cold gas via interaction with the intracluster medium (ram-pressure stripping), or with the parent halo, or with other galaxies (tidal interaction, harassment) and (ii) by reducing the rate at which the galaxies accrete the gas from their haloes (strangulation).

A number of observational studies show that galaxies in dense regions are redder and have lower star formation rate than those in the field (Kennicutt 1983; Balogh et al. 1999; Poggianti et al. 1999; Lewis et al. 2002; Gómez et al. 2003; Kauffmann et al. 2004; Bamford et al. 2009; Cooper et al. 2010; Peng et al. 2010, 2012; Schaefer et al. 2017), with galaxies in dense regions invariably showing H I deficiency (Davies & Lewis 1973; Haynes, Giovanelli & Chincarini 1984; Giovanelli & Haynes 1985; Solanes et al. 2001; Cortese et al. 2011; Catinella et al. 2013; Odekon et al. 2016; Stark et al. 2016; Brown et al. 2017; Li et al. 2020; Cortese, Catinella & Smith 2021), and gas-rich galaxies most often being found in weakly clustered regions (Meyer et al. 2007; Martin et al. 2012).

Since galaxy evolutionary pathways are affected by gravitational and hydrodynamical interactions with haloes, the position of a galaxy relative to the centre of its halo is important. In practice, the centre is often defined as the position of the most massive galaxy or the luminosity-weighted centre for all group members and, in recent years, significant effort has been invested into exploring the correlation between galaxy properties and group-centric radius. Using galaxy group catalogues based on the Sloan Digital Sky Survey (SDSS; York et al. 2000) Data Release 7 (DR7; Abazajian et al. 2009), Wetzel, Tinker & Conroy (2012) conclude that the quenched galaxy fraction increases at smaller group-centric radii. Bluck et al. (2016) quantify the impact that various environmental and galactic properties have on the quenching of star formation, using a sample of $\sim$ 400 000 centrals and $\sim$ 100 000 satellites from SDSS 7. They find that the group-centric radius has a significant impact on the

★ E-mail: wkhu@nao.cas.cn (WH); luca.cortese@uwa.edu.au (LC); lister.staveley-smith@uwa.edu.au (LS-S)

quenched fraction at fixed central velocity dispersion, with smaller group-centric radius being associated with a higher quenched fraction. Wang et al. (2018) show that the correlation between the quenched fraction of centrals and the halo-centric radius is weak, while the quenched fraction of satellites, in a given halo mass bin, shows a decreasing trend from the group centre outward. However, when both stellar and halo mass are controlled, the quenched fractions of centrals and satellites are once again similar (albeit some differences remain; see Davies et al. 2019 and discussion therein).

As well as the information derived from optical bands, the knowledge of a galaxy's H I content, as the raw fuel for future star formation, is also critical in understanding the influence of environment on galaxy evolution. Observations of H I gas have the potential to reveal the removal of cold gas. However, it is difficult for the current generation of radio telescopes to directly measure the 21-cm emission of large galaxy samples across environments, so this approach is limited to low redshifts, and generally able to trace only gas-normal galaxies. Using the method of spectral stacking, we can push the measurement of H I gas content to higher redshifts. The technique combines a large number of rest-frame spectra extracted from the radio data with angular and redshift positions from optical catalogues. In this process, the noise is averaged down and a more significant, but averaged over a large sample of galaxies, spectral-line signal is recovered. By stacking a larger number of galaxies, considerable large effective survey volumes and much smaller cosmic variance can be obtained. These advantages make stacking a powerful and easy-to-use tool for statistical studies of H I properties as a function of environment (e.g. Fabello et al. 2012; Brown et al. 2017).

Odekon et al. (2016) used stacking and multiple linear regressions, presenting the distribution of H I content in nearby groups and clusters measured in the 70 per cent complete Arecibo Legacy Fast-ALFA (ALFALFA; Giovanelli et al. 2005) survey. They find that at fixed stellar mass, the late-type galaxies in the inner regions of groups lack H I compared with galaxies in a control region extending to 4.0 Mpc surrounding each group.

In this work, we use a stacking method to explore how the H I content and the specific star formation rate (sSFR) change with the group-centric radius. In Hu et al. (2019, hereafter Paper I, 2020a), we have developed an interferometric stacking technique to measure the H I content in galaxies and confirm that there is little evolution in cosmic H I density ($\Omega_{\rm HI}$) at low redshift ($z < 0.11$). This paper uses the same sample and technique to study the relation between H I content and group-centric radius.

This paper is organized as follows: Section 2 presents the observational data and the optical catalogue we used in this paper. In Section 3, we give a simple description of the stacking methodology. In Section 4, we measure the H I content in satellites with different group-centric radii. We discuss our results in Section 5 and give the summary in Section 6. Throughout this paper, we use the cosmological parameters $h = 0.7$, $\Omega_{\rm m} = 0.3$, and $\Omega_{\Lambda} = 0.7$.

2 SAMPLE

2.1 Radio data

The H I observations were conducted with the Westerbork Synthesis Radio Telescope (WSRT) in a strip in the SDSS South Galactic Cap ($21{\rm h} < {\rm RA} < 2{\rm h}$ and $10° < {\rm Dec.} < 16°$), during 2011 May to 2012 October. The data are fully described in Paper I. We used 351 h of telescope time to observe 36 individual pointings, with each pointing being observed for between 5 and 12 h. Due to bad data quality, data

from one of the pointings were discarded. The half-power beamwidth (HPBW) of WSRT is 35 arcmin, and the average synthesized beam size is 108 arcsec × 22 arcsec. The frequency for the reduced data ranges from 1.406 to 1.268 GHz, corresponding to a redshift range of $0.01 < z < 0.12$. The radio astronomy data reduction package MIRIAD (Sault, Teuben & Wright 1995) was used to reduce and calibrate the data. The reduced data cubes of each pointing have a size of $1° × 1°$ with resolution of 3 arcsec × 3 arcsec in pixel size and 0.15625 MHz in frequency channel.

2.2 SDSS

We use SDSS DR7 as the optical catalogue for our stacking analysis. In our cross-matching procedure, we first obtain the positions (redshift, RA, Dec.) of the optical galaxies, then we extract the spectra in the same positions in the radio data. By cross-matching the SDSS catalogue with our radio data, we obtain a sample of 1895 galaxies with a redshift range of $0.01 < z < 0.11$ and an average redshift of $\langle z \rangle = 0.066$.

2.3 Yang group catalogue

In this paper, we use a dark matter halo group catalogue (Yang et al. 2007, 2012) based on the galaxies in the SDSS main galaxy sample with redshift completeness of $C \geq 0.7$. The first Yang group catalogue derived from the SDSS DR4 (Yang et al. 2007) used 362 356 galaxies to identify groups in the redshift range $0.01 < z < 0.2$. Extending their analysis to SDSS DR7, the number of galaxies was increased to ∼599 300 (Yang et al. 2012). In this catalogue, the following iterative process is used to identify the dark matter haloes: (1) identification of the group centres; (2) calculation of the group luminosity; and (3) estimation of additional properties of the tentative group such as mass, size, and velocity dispersion. Based on the properties of the haloes, the group members might be reassigned. Afterwards, a new group centre is then defined and the process is iterated until the members of the groups are stable. The final halo masses are calculated using the halo mass function derived by Warren et al. (2006).

In this paper, the central galaxy is determined as the galaxy with highest stellar mass. Other galaxies in the group will be called satellites. The stellar masses and sSFR used in this paper are taken from the MPA–JHU (Max-Planck Institute for Astrophysics–John Hopkins University) value-added galaxy catalogue, which are derived from the SDSS DR7 catalogue (Kauffmann et al. 2003).

In this group catalogue, galaxies with a redshift completeness of $C \leq 0.7$ are excluded. The cross-matching of the SDSS DR7 sources contained within our pointings with the Yang catalogue (DR7) reduces the number of galaxies in the sample by ∼ 5 per cent from 1895 to 1793 galaxies, with an average redshift of $\langle z \rangle = 0.065$. The redshift and stellar mass distribution of satellites (red line), isolated galaxies (green line), centrals (blue line), and all galaxies (black line) are shown in Fig. 1. Most of the galaxies in our sample have a stellar mass of around $10^{10.5}$ M$_\odot$. In Fig. 2, we present the stellar mass distribution against redshift. This shows that our sample is magnitude-limited. We show the number of galaxies in bins of halo mass in Fig. 3. It shows that the median number of galaxies per halo increases with increasing halo mass. Groups with higher halo mass have more satellite galaxies.

Out of the 1793 galaxies included in the group catalogue, 350 do not have assigned halo masses as the Yang catalogue did not assign halo masses to small haloes. Among these galaxies, over 96 per cent are isolated centrals. For these galaxies in extremely small
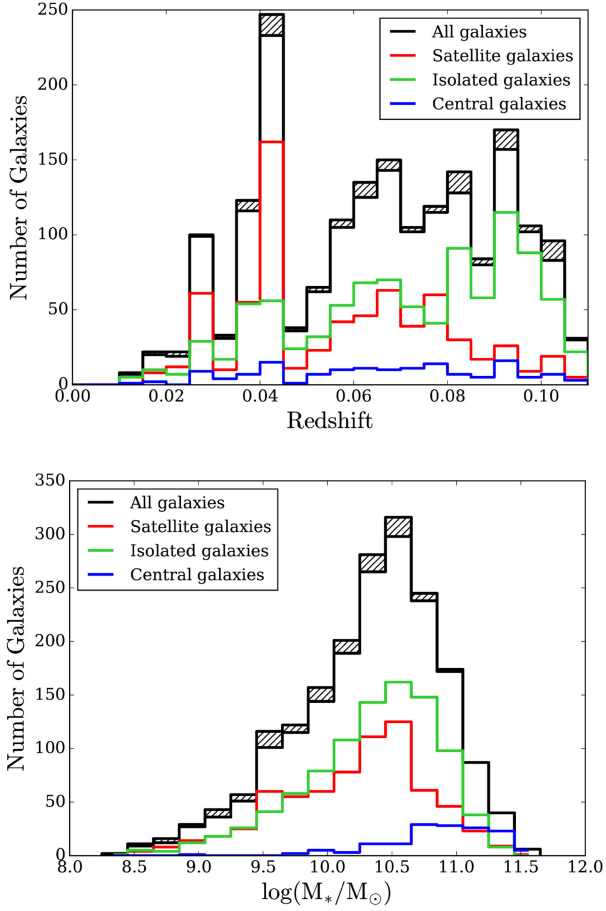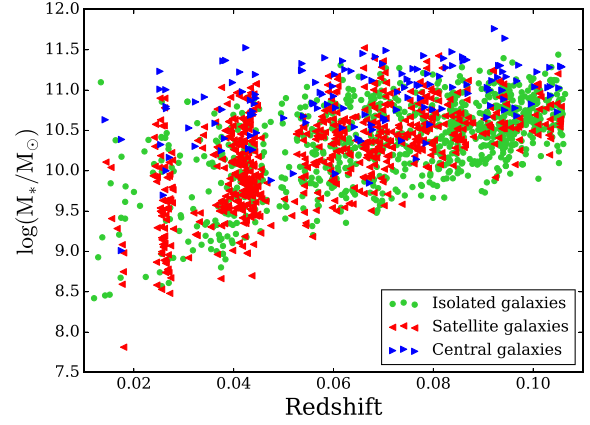
Figure 2. The stellar mass versus redshift distribution for the SDSS spectroscopic subsample contained within the 35 WSRT pointings. The satellite, group centrals, and isolated galaxies are showed by the red left triangles, blue right triangles, and green points, respectively.

Figure 1. Redshift (top panel) and stellar mass (bottom panel) distribution for the SDSS spectroscopic subsample contained within the 35 WSRT pointings. The distributions for all galaxies, satellite galaxies, isolated, and group central galaxies are shown by the black, red, green, and blue lines, respectively. The hatched region shows the galaxies not included in Yang catalogue. The group catalogue is based on the main galaxy sample from SDSS DR7 and galaxies with a redshift completeness of $C \leq 0.7$ are removed. The missing galaxies tend to be low mass and faint. The interval for stellar mass bins and redshift bins are 0.2 dex and 0.005, respectively. The lower limit of the redshift of the selected sample is $z = 0.01$, and the upper limit of the redshift is $z = 0.11$. The average redshift of the sample is $\langle z \rangle = 0.065$.

halo mass groups, we estimate their halo masses by solving the following equation (Yang, Mo & van den Bosch 2009):

$$\langle M_* \rangle (M_{\rm h}) = M_0 \frac{(M_{\rm h}/M_1)^{\alpha+\beta}}{(1 + M_{\rm h}/M_1)^{\beta}}, \qquad (1)$$

where M_* is the stellar mass of the central galaxies, $M_{\rm h}$ is the halo mass, and M_1 is a characteristic halo mass. The parameters obtained from the SDSS groups are: $\alpha = 0.315$, $\beta = 4.543$, $\log M_0 = 10.306$, and $\log M_1 = 11.040$, where M_0 is in units of $h^{-2}\,{\rm M}_\odot$ and M_1 in $h^{-1}\,{\rm M}_\odot$.

Across the sample, 699 (39 per cent) galaxies are classified as satellite galaxies while 1094 (61 per cent) galaxies are classified as central galaxies, among which 906 galaxies are isolated. In the following calculation, we will consider the central galaxies and isolated galaxies separately. In order to make sure that we are tracing environment instead of simple selection biases, we account for galaxy type and stellar mass by limiting the mass range to $10.0 < \log(M_*/{\rm M}_\odot) < 11.5$ when comparing H I properties in the
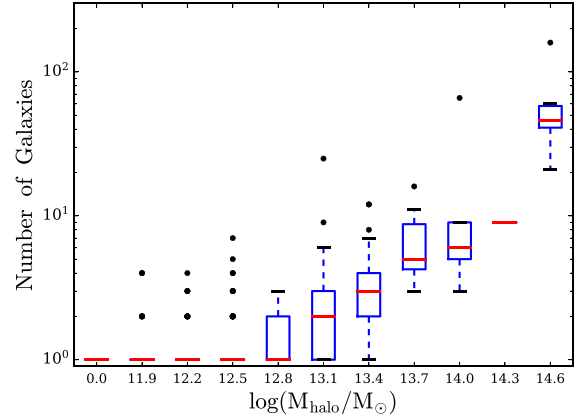
Figure 3. Box-and-whisker plot of number of galaxies in a halo of a certain mass. The width of halo mass bins is 0.3 in log scale. The red line indicates the mean number of galaxies in a halo and the box marks the first and third quartile of the data, while the whiskers mark the lowest and highest value still within 1.5 times the interquartile range. The outliers are marked as individual black dots. The figure shows that the median number of galaxies per halo increases with increasing halo mass and that the range in number of galaxies gets broader. Note that $\log M_{\rm halo} = 0$ means that no mass was assigned to that halo.

inner and outer regions of groups. We also create a subsample that only contains the late-type galaxies to quantify the influence from morphology. We separate galaxies by the morphology using the r-band inverse concentration index, which is defined as the ratio of the radii containing 50 per cent (r_{50}) to that containing 90 per cent (r_{90}) of the Petrosian flux. Galaxies with r_{50}/r_{90} larger than 0.33 are classified as late type (Shimasaku et al. 2001). In Fig. 4, we present the stellar mass distribution against inverse concentration index. As expected, early-type galaxies tend to have larger stellar mass. The orange dashed line shows the morphological selection we used. The mass-limited subsample contains 466 satellite galaxies and 723 isolated galaxies, among which 457 (344 for the late-type subsample) satellites with group-centric radius $R < R_{180}$ and 120 (90 for the late-type subsample) isolated galaxies in the infalling region
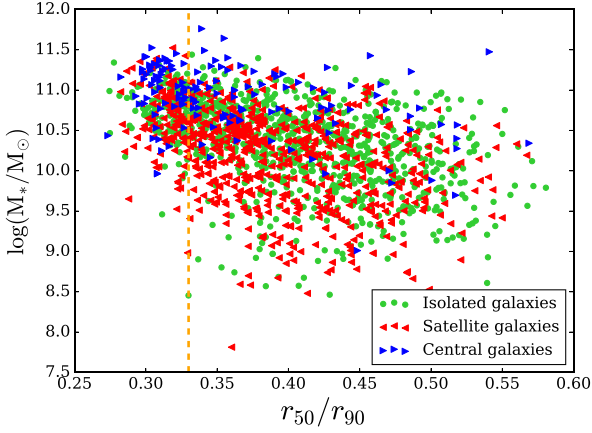
Figure 4. Same as Fig. 2 but for the stellar mass versus inverse concentration index distribution. The orange dashed line shows the morphological selection we use (inverse concentration index $r_{50}/r_{90} = 0.33$).

(see the definition in Section 4.2) are used in the following to quantify the H I content of galaxies as a function of group-centric radius.

Limited by the size of the WSRT primary beam, some groups have not been mapped out to their virial radius. Specifically, out of a total of 236 groups (120 isolated galaxies included) in the mass-limited sample, 23 groups are partially observed. This will limit our H I measurement at large group-centric radius but the relationship between H I properties and group-centric radius should not be affected.

3 STACKING SCRIPT

3.1 Main procedure

The stacking technique applied in this work is described in detail in Paper I. Here, we provide a short summary of the key steps. The spectra for galaxies were extracted from the radio data cubes over an extended region with aperture radius of 35 kpc around the SDSS position. After removing the residual continuum emission from bright sources, the spectra were de-redshifted to rest frame and the H I flux density is conserved via using $S_{\nu_{res}} = S_{\nu_{obs}}/(1 + z)$. The mass spectra were calculated using

$$m_{HI}(\nu) = 4.98 \times 10^7 S_\nu D_L^2 f^{-1}, \tag{2}$$

where S_ν is the de-redshifted H I flux density in Jy, D_L refers to the luminosity distance in units of Mpc, f denotes the normalized primary beam response, and m_{HI} is in units of $M_\odot$ MHz^{-1}. The spectrum of i-th galaxy is weighted by

$$w_i = f^2 D_L^{-1} \sigma^{-2}, \tag{3}$$

where σ is the rms noise of the flux density spectra. The final averaged stacked spectrum is calculated by

$$\langle m_{HI}(\nu) \rangle = \frac{\sum_{i=1}^{n} w_i m_{HI,i}}{\sum_{i=1}^{n} w_i}. \tag{4}$$

The integrated H I mass of a stack can be obtained by integrating the mass spectrum along the frequency axis:

$$\langle M_{HI} \rangle = \int \langle m_{HI}(\nu) \rangle d\nu, \tag{5}$$

where the integration region is $\sim \pm 1.5$ MHz and will be slightly adjusted to exclude external noise and signal.

The error of the H I mass measurement is estimated by jackknife resampling. 5 per cent of the sample are excluded when we do the jackknife resampling. The H I mass fraction $\langle M_{HI}/M_* \rangle$ and its error can also be measured by stacking the individual M_{HI}/M_* spectra. This is done via equations (4) and (5), with M_{HI} replaced by M_{HI}/M_*.

3.2 Confusion correction

The value of the average H I mass we measure via the stacking method may be artificially inflated by the effect of beam confusion. Flux from objects with a projected distance smaller than the WSRT synthesized beam and line-of-sight velocity difference lower than the spectral extraction region cannot be distinguished. Additional H I signal from nearby galaxies can therefore contaminate the measurements. We define confused galaxies as SDSS galaxies having one or more companions within the WSRT synthesized beam, and within 3 MHz (~ 630 km s^{-1} at $z = 0$) in frequency. No stellar mass cut is applied when we select the confused galaxies. Although the WSRT synthesized beam is small, ~ 7 per cent of our whole sample is potentially confused with neighbouring galaxies. Directly removing confused galaxies will have the effect of removing massive centrals and gas-rich satellites. To correct for the effects of confusion in these galaxies without introducing bias, we follow the method in Fabello et al. (2012) and Hu et al. (2020a), where the total signal S_i is estimated as the sum of the signal of the sample galaxy (S_s) and the signal of the companions (S_c) weighted with two overlap factors:

$$S_i = S_s + \Sigma_c f_{1;c} f_{2;c} S_c, \tag{6}$$

where the f_1 and f_2 model the overlap between the sample galaxy and its companion in angular and redshift space. The expected H I mass of each companion is estimated using the M_{HI} versus galaxy optical diameter relation (Toribio et al. 2011). The true signal of the sample galaxy is obtained by

$$S_s = S_i - \Sigma_c f_{1;c} f_{2;c} S_c. \tag{7}$$

The confusion correction will be later applied to all confused galaxies in all stacking, by subtracting the signal from the companion before the final weighting is applied (equation 4):

$$m_{HI}^s(\nu) = m_{HI}^i(\nu) - \Sigma_c m_{HI}^c(\nu), \tag{8}$$

where $m_{HI}^s(\nu)$ refers to the true H I mass spectrum from the sample galaxy, $m_{HI}^i(\nu)$ contains total H I signal and $m_{HI}^c(\nu)$ is the estimated H I signal from companion and $\int_{-\Delta\nu}^{\Delta\nu} \langle m_{HI}(\nu) \rangle d\nu = f_{1;c} f_{2;c} S_c$. The true H I mass spectrum, $m_{HI}^s(\nu)$, is the spectrum we will use in the following stacking (in other words, $m_{HI,i}$ in equation 4).

We do not see a clear dependence of the H I-confused fraction on redshift. Nearly the same stacking results and H I properties-projected distance relations are obtained, when only galaxies classified as non-confused are included in the analysis. However, to take full advantage of our large number statistics, in the rest of this paper we include confused galaxies and apply the method described above to correct the confusion.

4 H I CONTENT BINNED BY GROUP-CENTRIC RADIUS

In this section, we present the H I content versus group-centric radius relations. In the Yang catalogue, the dark matter haloes are defined as having an overdensity of 180, so the halo radius at which the average enclosed density is 180 times the critical density can be obtained
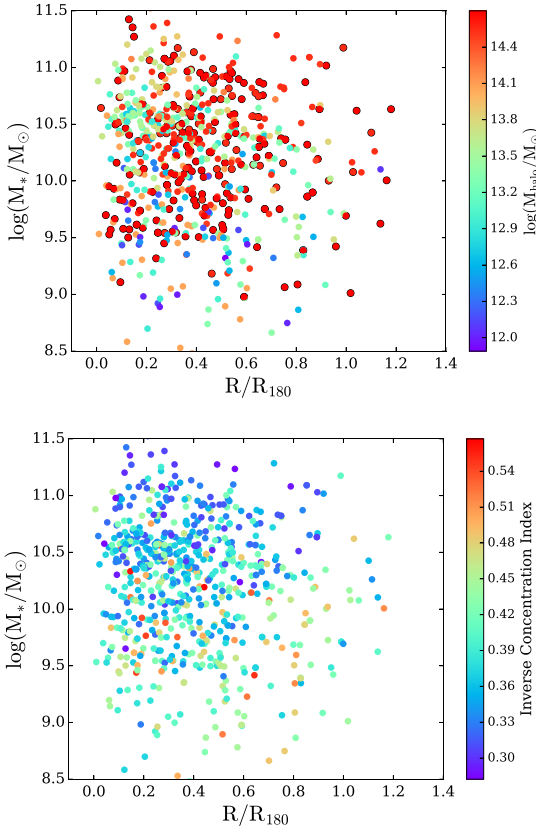
Figure 5. Stellar mass as a function of normalized projected group-centric radius for satellites, coloured according to the halo mass of the group the satellites are located in (upper panel) and their inverse concentration index (lower panel). The points with black circles refer to the satellites from the two largest groups.

from

$$R_{180} = 0.781\, h^{-1}\, \mathrm{Mpc} \left(\frac{M_{\mathrm{h}}}{\Omega_{\mathrm{m}} 10^{14}\, h^{-1}\, \mathrm{M_\odot}} \right)^{1/3} (1 + z_{\mathrm{group}})^{-1}, \quad (9)$$

where M_{h} is the mass of the group the satellite is located in and z_{group} is the redshift of the group centre. Using the technique described in Section 3, we can measure the H I content in galaxies with different normalized projected group-centric radii.

Fig. 5 shows stellar mass as a function of normalized projected group-centric radius for satellites, coloured according to the halo mass of the group that the satellites are located in (upper panel) and their inverse concentration index (lower panel). Except for the satellites in the two largest groups (labelled with black circles), the high-mass galaxies are more likely to be found in high-mass groups. We should note that H I mass, H I gas fraction, and H I deficiency depend strongly on stellar mass, as shown in Odekon et al. (2016) and Catinella et al. (2018). If stellar mass is not controlled, the measured H I properties versus group-centric radius relations will be affected by the relations between stellar mass and radius. In order to incorporate stellar mass as an additional independent variable and make use of as many galaxies as possible, we select the satellites by their stellar masses in the range $10^{10.0} < M_*/\mathrm{M_\odot} \leq 10^{11.5}$. The lower panel of Fig. 5 shows that the high-mass galaxies are more likely to have lower inverse concentration index and no clear relation between group-centric radius and morphology is found. In order to quantify the influence from galaxy type, we select the late-type

satellites with inverse concentration index larger than 0.33 and carry out the measurement with only the late-type galaxies.

The measured relations between H I content and group-centric radius are shown in Fig. 6 and Table 1. The stacked mass spectra for satellite galaxies are shown in Appendix (Fig. A1). In Table 1, we also present the inverse concentration index (labelled as r_{50}/r_{90}) and stacked stellar mass as a function of radius. The average stellar mass of satellites slightly decreases with increasing group distance for the first four bins. Given that H I mass generally increases with stellar mass, if stellar mass is driving our results we should find higher gas masses closer to the group centre. Conversely, for the stacks within $R/R_{180} \sim 0.8$, we find that at fixed stellar mass, satellite galaxies in the inner region lack H I compared to galaxies in the outer region of each group. For the average H I mass fraction, satellite galaxies in the inner region have lower values relative to satellites in the outer regions. The dependence of H I content and H I gas fraction on distance from the group centre for satellites at fixed stellar mass likely reflects the mechanism for removing gas in the inner regions.

For comparison, we stack the sSFR for the same sample using the same method, with H I mass spectra replaced by sSFR, and show the results in the right-hand panel of Fig. 6. This shows that satellites in the outer regions of groups have higher sSFRs than those at small group-centric radii. The sSFR in the last bin is lowest because those galaxies have highest averaged stellar mass.

For the late-type subsample, the same trends are found but with higher average H I mass, H I mass fraction, and sSFR values in all except the last radial bins. We note that the average stellar mass of the late-type satellites is lower ($\sim 3.7 \times 10^{10}\, \mathrm{M_\odot}$) and changes little with increasing group distance for the first four bins. For both of the all-type and the late-type sample, the average inverse concentration index of satellites changes little with increasing group distance, indicating that our results are not influenced by the morphology of galaxies.

4.1 Environmental dependence

To study the physical mechanism behind the H I properties versus group-centric radius relations, we further bin the satellites by the halo mass of groups in which they are located, or by projected density, and compare the results obtained with these two different environmental metrics.

4.1.1 Group halo mass

We split the satellites in the stellar mass range $10^{10.0} < M_* \leq 10^{11.5}\, \mathrm{M_\odot}$ into two subsamples according to the mass of the group in which they reside: $M_{\mathrm{halo}} \leq 10^{13.5}\, h^{-1}\, \mathrm{M_\odot}$ and $M_{\mathrm{halo}} > 10^{13.5}\, h^{-1}\, \mathrm{M_\odot}$. There are 90 (79 for the late-type subsample) groups and 25 (24 for the late-type subsample) groups in these two subsamples, respectively. The low-mass and high-mass group subsamples have an averaged halo mass of $(1.41 \pm 1.07) \times 10^{13}$ and $(1.54 \pm 1.44) \times 10^{14}\, \mathrm{M_\odot}$, respectively [$(1.40 \pm 1.07) \times 10^{13}$ and $(1.58 \pm 1.45) \times 10^{14}\, \mathrm{M_\odot}$ for the late-type subsample].

We show the stacked H I mass, H I gas fraction, and sSFR in different radial bins in Fig. 7 and Table 2. The average stellar mass from stacks of subsamples in the first several radial bins is similar, both for high-mass groups and low-mass groups. For the high-mass group subsample, the last radial bin was extended to 1.2 R_{180} to contain more galaxies and improve statistics.

We find a monotonic decrease of H I mass in satellite galaxies with decreasing distance from the centre of the group for both low- and
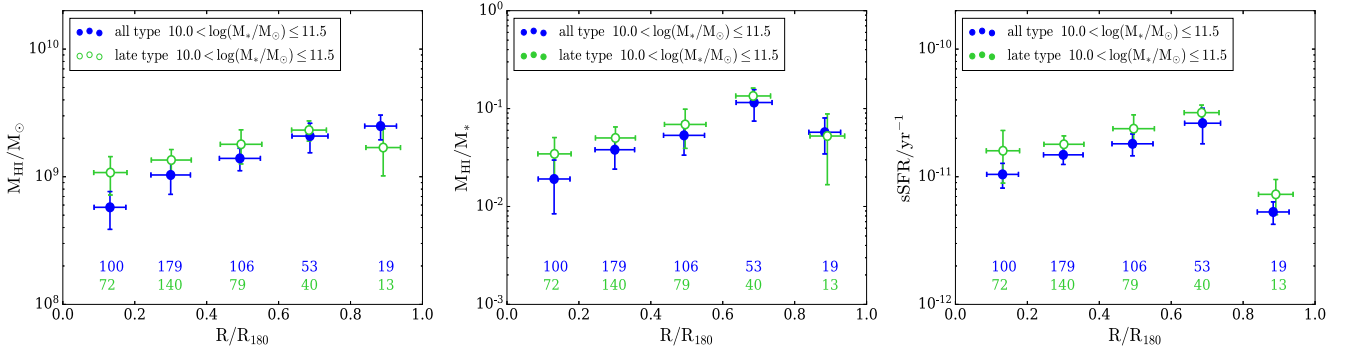
Figure 6. Averaged H I mass (left-hand panel), H I mass fraction (middle panel), and specific star formation rate (right-hand panel) for the all-type (blue filled points) and the late-type (green open points) satellites with stellar mass: $10^{10.0} < M_* \leqslant 10^{11.5}$ M$_\odot$, as a function of normalized projected group-centric radius. The error bars are estimated using jack-knife resampling. The numbers below the points show the number of galaxies in each radial bin. The corresponding values are presented in Table 1.

Table 1. Stacked H I properties as a function of group-centric radius for satellites with $10^{10.0} < M_* \leq 10^{11.5}$ M$_\odot$. We illustrate the results in Fig. 6.

| Radius bin (R_{180})	Radius (R_{180})	Number of galaxies	r_{50}/r_{90}	$\langle M_* \rangle$ ($10^{10}\,h_{70}^{-2}$ M$_\odot$)	$\langle M_{\rm HI} \rangle$ ($10^9\,h_{70}^{-2}$ M$_\odot$)	$\langle M_{\rm HI}/M_* \rangle$	$\langle {\rm sSFR} \rangle$ (10^{-11} yr^{-1})
All type							
(0.0,0.2]	0.13 ± 0.04	100	0.37 ± 0.05	4.8 ± 0.6	0.6 ± 0.2	0.02 ± 0.01	1.0 ± 0.2
(0.2,0.4]	0.30 ± 0.05	179	0.38 ± 0.06	4.5 ± 0.3	1.0 ± 0.3	0.04 ± 0.01	1.5 ± 0.2
(0.4,0.6]	0.49 ± 0.06	106	0.37 ± 0.06	4.3 ± 0.4	1.4 ± 0.3	0.05 ± 0.02	1.8 ± 0.3
(0.6,0.8]	0.69 ± 0.05	53	0.38 ± 0.06	3.6 ± 0.5	2.1 ± 0.5	0.12 ± 0.04	2.6 ± 0.8
(0.8,1.0]	0.88 ± 0.04	19	0.37 ± 0.06	5.3 ± 1.1	2.5 ± 0.5	0.06 ± 0.02	0.5 ± 0.1
Late type							
(0.0,0.2]	0.13 ± 0.05	72	0.39 ± 0.05	3.6 ± 0.3	1.1 ± 0.3	0.03 ± 0.02	1.6 ± 0.5
(0.2,0.4]	0.30 ± 0.05	140	0.39 ± 0.05	3.8 ± 0.3	1.4 ± 0.3	0.05 ± 0.01	1.8 ± 0.3
(0.4,0.6]	0.49 ± 0.06	79	0.40 ± 0.05	3.7 ± 0.4	1.8 ± 0.5	0.07 ± 0.03	2.4 ± 0.6
(0.6,0.8]	0.68 ± 0.05	40	0.40 ± 0.05	3.3 ± 0.4	2.3 ± 0.4	0.13 ± 0.03	3.2 ± 0.5
(0.8,1.0]	0.89 ± 0.05	13	0.40 ± 0.05	4.2 ± 1.1	1.7 ± 0.7	0.05 ± 0.03	0.7 ± 0.2
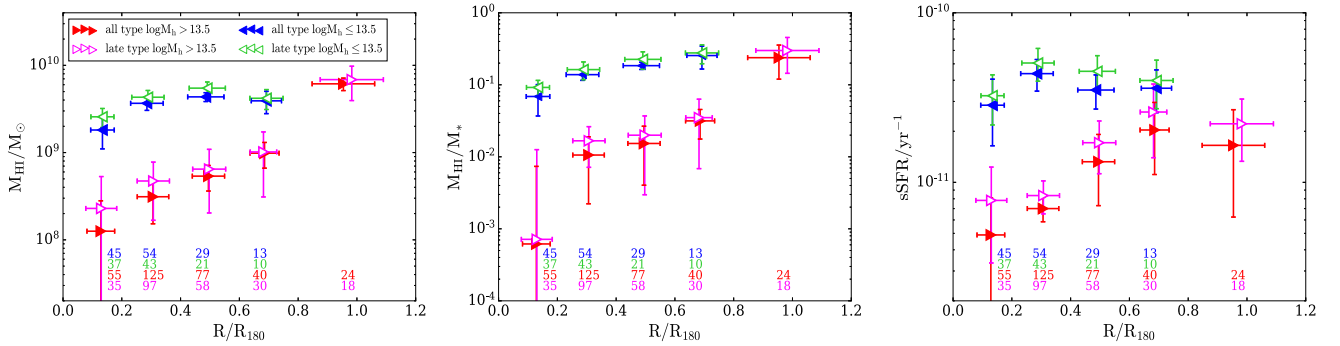
Figure 7. Same as Fig. 6, with satellite galaxies in $10^{10.0} < M_* \leqslant 10^{11.5}$ M$_\odot$ divided into two group halo mass bins, above and below $10^{13.5}\,h^{-1}$ M$_\odot$ (right-pointing and left-pointing triangles), respectively. The results from the all-type and the late-type satellites are labelled as filled and open points, respectively. The corresponding values are presented in Table 2.

high-mass groups, with high-mass groups showing a more dramatic drop in gas content.

For satellites in high-mass groups, the H I content residing in the most inner parts ($R \sim 0.13\,R_{180}$) of groups is $\sim$60 times smaller than that in the outer parts ($R \sim 0.95\,R_{180}$). It is worth stressing that, in the inner parts of high-mass groups, the H I content residing in satellites is less than in low-mass groups, even though the average stellar masses are higher in the former. This

indicates that the gas removal process is more active in higher mass groups.

Similar trends apply to H I gas fraction and sSFR, although in the case of gas fraction the trend is noisier due to the fact that for two more radial bins the stacking results are more uncertain. Specifically, we do not detect H I in the first radial bin, and we have marginal detections (signal-to-noise ratio lower than 3) in the third and fourth radial bins.

Table 2. Stacked H I properties as a function of group-centric radius for satellites with $10^{10.0}\,\mathrm{M_\odot} < M_* \le 10^{11.5}\,\mathrm{M_\odot}$ in two bins of group halo mass. We illustrate the results in Fig. 7.

Radial bins (R_{180})	Radius (R_{180})	Number of galaxies	r_{50}/r_{90}	$\langle M_* \rangle$ $(10^{10}\,h_{70}^{-2}\,\mathrm{M_\odot})$	$\langle M_{\mathrm{H\,I}} \rangle$ $(10^{9}\,h_{70}^{-2}\,\mathrm{M_\odot})$	$\langle M_{\mathrm{H\,I}}/M_* \rangle$	$\langle \mathrm{sSFR} \rangle$ $(10^{-11}/\mathrm{yr}^{-1})$
Low-mass group: $M_{\mathrm{halo}} \leqslant 10^{13.5}\,h^{-1}\,\mathrm{M_\odot}$, all type							
(0.0,0.2]	0.13 ± 0.04	45	0.39 ± 0.06	3.4 ± 0.2	1.8 ± 0.7	0.07 ± 0.03	2.8 ± 1.2
(0.2,0.4]	0.29 ± 0.05	54	0.39 ± 0.06	3.6 ± 0.7	3.7 ± 0.6	0.14 ± 0.02	4.4 ± 0.9
(0.4,0.6]	0.49 ± 0.06	29	0.38 ± 0.06	3.4 ± 0.7	4.3 ± 0.5	0.18 ± 0.02	3.5 ± 0.8
(0.6,0.8]	0.69 ± 0.05	13	0.40 ± 0.07	2.2 ± 0.2	3.9 ± 1.1	0.25 ± 0.08	3.6 ± 1.0
High-mass group: $M_{\mathrm{halo}} > 10^{13.5}\,h^{-1}\,\mathrm{M_\odot}$, all type							
(0.0,0.2]	0.13 ± 0.05	55	0.35 ± 0.04	5.2 ± 0.8	0.1 ± 0.2	0.001 ± 0.007	0.5 ± 0.3
(0.2,0.4]	0.31 ± 0.05	125	0.37 ± 0.05	5.0 ± 0.3	0.3 ± 0.2	0.011 ± 0.008	0.7 ± 0.1
(0.4,0.6]	0.49 ± 0.05	77	0.37 ± 0.05	4.7 ± 0.3	0.5 ± 0.2	0.015 ± 0.011	1.3 ± 0.6
(0.6,0.8]	0.69 ± 0.05	40	0.37 ± 0.05	4.1 ± 0.6	1.0 ± 0.3	0.032 ± 0.014	2.0 ± 0.9
(0.8,1.2]	0.95 ± 0.11	24	0.38 ± 0.06	4.8 ± 0.3	6.1 ± 1.0	0.238 ± 0.118	1.7 ± 1.0
Low-mass group: $M_{\mathrm{halo}} \leqslant 10^{13.5}\,h^{-1}\,\mathrm{M_\odot}$, late type							
(0.0,0.2]	0.13 ± 0.04	37	0.41 ± 0.05	3.2 ± 0.3	2.6 ± 0.6	0.09 ± 0.02	3.2 ± 1.1
(0.2,0.4]	0.29 ± 0.05	43	0.41 ± 0.06	3.5 ± 0.3	4.3 ± 0.8	0.16 ± 0.04	5.1 ± 1.1
(0.4,0.6]	0.49 ± 0.06	21	0.41 ± 0.05	3.0 ± 0.4	5.5 ± 0.9	0.23 ± 0.06	4.5 ± 1.1
(0.6,0.8]	0.69 ± 0.05	10	0.43 ± 0.06	2.2 ± 0.3	4.2 ± 1.0	0.28 ± 0.08	4.0 ± 1.2
High-mass group: $M_{\mathrm{halo}} > 10^{13.5}\,h^{-1}\,\mathrm{M_\odot}$, late type							
(0.0,0.2]	0.13 ± 0.05	35	0.37 ± 0.04	3.7 ± 0.6	0.2 ± 0.3	0.001 ± 0.012	0.8 ± 0.4
(0.2,0.4]	0.31 ± 0.05	97	0.39 ± 0.04	4.1 ± 0.2	0.5 ± 0.3	0.017 ± 0.009	0.8 ± 0.2
(0.4,0.6]	0.50 ± 0.06	58	0.39 ± 0.04	4.0 ± 0.4	0.6 ± 0.4	0.020 ± 0.017	1.7 ± 0.6
(0.6,0.8]	0.68 ± 0.04	30	0.39 ± 0.04	3.6 ± 0.9	1.0 ± 0.7	0.035 ± 0.028	2.6 ± 1.2
(0.8,1.2]	0.98 ± 0.11	18	0.40 ± 0.05	3.8 ± 1.3	6.8 ± 3.0	0.299 ± 0.155	2.2 ± 0.9

Similar trends are found for the late-type subsample at fixed stellar mass, but with higher average H I mass, H I mass fraction, and sSFR values in nearly all radial bins.

4.1.2 Projected density

We also consider the local density as an environment metric and measure the H I content versus group-centric radius relations in subsamples of different local projected densities. To calculate the local projected density (Σ), we count the number of neighbouring SDSS galaxies per projected Mpc^2. The galaxies are limited to those within the redshift range of each group. We then split the satellites into two subsamples with local density $\Sigma > 5$ and $\Sigma \le 5$ Mpc^{-2}. For stacking purposes, we again only use the satellites with $10^{10.0} < M_* \leqslant 10^{11.5}\,\mathrm{M_\odot}$ and limit our measurement to the late-type galaxies. The low-density and high-density subsamples have an averaged local density of (2.87 ± 0.85) and (13.07 ± 9.52) Mpc^{-2} [(2.88 ± 0.81) Mpc^{-2} and (12.33 ± 8.83) Mpc^{-2} for the late-type satellites], respectively.

We stack the H I mass, H I gas fraction, and sSFR of satellites in different radial bins and show the results in Fig. 8 and Table 3. Low densities ($\Sigma \le 5$ Mpc^{-2}) and high densities ($\Sigma > 5$ Mpc^{-2}) are indicated in blue and red, respectively. Table 3 shows that the average stellar mass changes little with group-centric radius, for the first three radial bins.

The relation between average H I mass and projected radius clearly depends on the local densities. At a fixed stellar mass, inner satellites in high-density regions lack H I relative to galaxies in the outer region of each density group. However, satellites in low-density regions show no change of H I content with radius. Similar results are obtained if we plot gas fractions instead of gas masses. This suggests that H I removal is radially dependent only in relatively high density regions within groups.

Stacks of sSFR show that the satellites in higher density regions have lower sSFR at fixed stellar mass. For satellites in lower density environments, a radial trend with group-centric radius may still be present, but only within $R \sim 0.3\,R_{180}$.

Similar results are obtained for the late-type subsample but with more moderate increasing trends with radius.

4.2 Extending to larger distances

Using stacking and multiple linear regressions, Odekon et al. (2016) presented the H I content distribution in nearby groups and clusters measured by the 70 per cent-complete ALFALFA survey. They found that at fixed stellar mass, the late-type galaxies in the inner parts of groups lack H I compared with galaxies in a control region extending to 4.0 Mpc surrounding each group. The effect is detectable in groups with $M_{200} \lesssim 10^{14.5}\,\mathrm{M_\odot}$ as well as in clusters ($M_{200} \gtrsim 10^{14.5}\,\mathrm{M_\odot}$), which indicates pre-processing of H I gas in intermediate-density isolated groups.

Motivated by these findings, we extend our analysis to higher group-centric radii by searching for isolated galaxies around each group. The distribution of galaxies in groups depends on their orbital and infall history, and can be modelled by phase-space diagrams (Mahajan, Mamon & Raychaudhury 2011; Oman, Hudson & Behroozi 2013; Oman & Hudson 2016; Pasquali et al. 2019), which use both projected group-centric velocity and projected group-centric radius. The range of the positions of satellites in groups can be defined by a caustic profile (Pasquali et al. 2019): $K = |\Delta V|/\sigma \times R/R_{180}$, where $|\Delta V|$ is the peculiar line-of-sight velocity and σ is the velocity dispersion along the line of sight, which is obtained by computing the standard unbiased variance of the line-of-sight velocities. The value of K will change with the infall time of the satellites, with ancient infallers having smaller values compared to recent infallers (Pasquali et al. 2019).
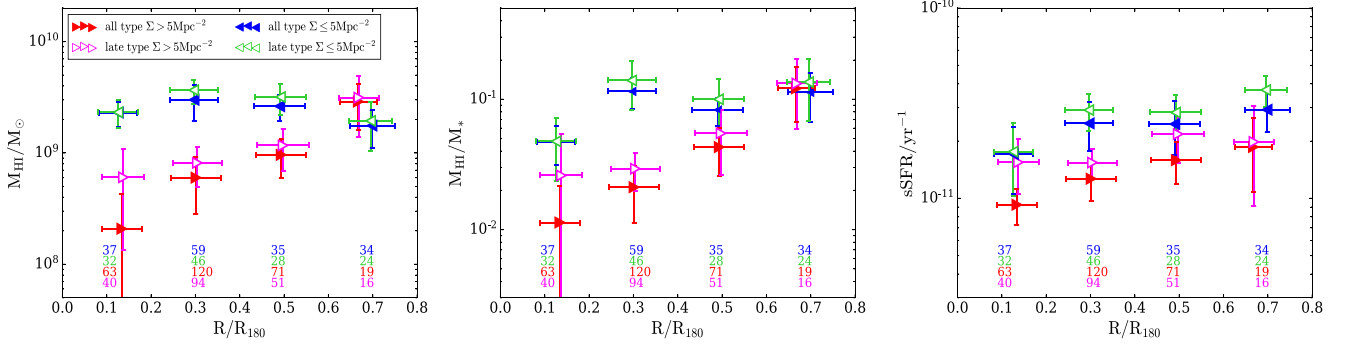
Figure 8. Same as Fig. 6, with satellite galaxies in $10^{10.0} < M_* \leqslant 10^{11.5}\,\mathrm{M_\odot}$ divided into two local density bins, above and below 5 Mpc^{-2} (right-pointing and left-pointing triangles), respectively. The corresponding values are presented in Table 3.

Table 3. Stacked H I properties as a function of group-centric radius for satellites with $10^{10.0}\,\mathrm{M_\odot} < M_* \leq 10^{11.5}\,\mathrm{M_\odot}$ in two bins of local density. We illustrate the results in Fig. 8.

Radial bins (R_{180})	Radius (R_{180})	Number of galaxies	r_{50}/r_{90}	$\langle M_* \rangle$ $(10^{10}\,h_{70}^{-2}\,\mathrm{M_\odot})$	$\langle M_{\mathrm{H\,I}} \rangle$ $(10^9\,h_{70}^{-2}\,\mathrm{M_\odot})$	$\langle M_{\mathrm{H\,I}}/M_* \rangle$	$\langle \mathrm{sSFR} \rangle$ $(10^{-11}/\mathrm{yr}^{-1})$
Low density: $\Sigma \leq 5$ Mpc^{-2}, all type							
(0.0,0.2]	0.13 ± 0.04	37	0.39 ± 0.06	4.1 ± 0.5	2.3 ± 0.6	0.05 ± 0.02	1.7 ± 0.6
(0.2,0.4]	0.30 ± 0.05	59	0.39 ± 0.06	4.5 ± 0.3	3.0 ± 1.1	0.11 ± 0.03	2.5 ± 0.7
(0.4,0.6]	0.49 ± 0.06	35	0.38 ± 0.05	4.0 ± 0.6	2.6 ± 0.7	0.08 ± 0.02	2.5 ± 0.8
(0.6,0.8]	0.70 ± 0.05	34	0.38 ± 0.06	3.5 ± 0.5	1.8 ± 0.6	0.11 ± 0.04	2.9 ± 0.7
High density: $\Sigma > 5$ Mpc^{-2}, all type							
(0.0,0.2]	0.13 ± 0.04	63	0.36 ± 0.04	4.9 ± 0.8	0.2 ± 0.2	0.011 ± 0.010	0.9 ± 0.2
(0.2,0.4]	0.30 ± 0.05	120	0.37 ± 0.05	4.5 ± 0.4	0.6 ± 0.3	0.021 ± 0.009	1.3 ± 0.3
(0.4,0.6]	0.49 ± 0.06	71	0.37 ± 0.06	4.5 ± 0.3	1.0 ± 0.4	0.043 ± 0.017	1.6 ± 0.4
(0.6,0.8]	0.67 ± 0.04	19	0.38 ± 0.05	3.3 ± 0.1	2.9 ± 1.2	0.121 ± 0.054	1.9 ± 0.7
Low density: $\Sigma \leq 5$ Mpc^{-2}, late type							
(0.0,0.2]	0.13 ± 0.04	32	0.41 ± 0.05	4.2 ± 0.6	2.3 ± 0.6	0.05 ± 0.02	1.8 ± 0.7
(0.2,0.4]	0.30 ± 0.05	46	0.40 ± 0.05	4.1 ± 0.7	3.7 ± 0.9	0.14 ± 0.06	2.9 ± 0.6
(0.4,0.6]	0.49 ± 0.06	28	0.40 ± 0.04	3.2 ± 0.3	3.2 ± 0.9	0.10 ± 0.04	2.8 ± 0.7
(0.6,0.8]	0.70 ± 0.05	24	0.40 ± 0.05	3.1 ± 0.6	1.9 ± 0.9	0.14 ± 0.06	3.7 ± 0.7
High density: $\Sigma > 5$ Mpc^{-2}, late type							
(0.0,0.2]	0.14 ± 0.05	40	0.38 ± 0.04	3.2 ± 0.4	0.6 ± 0.5	0.026 ± 0.028	1.5 ± 0.5
(0.2,0.4]	0.30 ± 0.05	94	0.39 ± 0.05	3.6 ± 0.3	0.8 ± 0.3	0.029 ± 0.010	1.5 ± 0.3
(0.4,0.6]	0.50 ± 0.06	51	0.39 ± 0.05	4.0 ± 0.4	1.2 ± 0.5	0.055 ± 0.028	2.2 ± 0.6
(0.6,0.8]	0.67 ± 0.04	16	0.39 ± 0.04	3.5 ± 0.2	3.1 ± 1.7	0.132 ± 0.072	2.0 ± 1.0

Using cosmological hydrodynamic *N*-body simulations of groups and clusters, Rhee et al. (2017) investigate how the information on environmental effects acting in groups and clusters can be extracted by the knowledge of locations in phase-space coordinates. They show that galaxies tend to follow a typical path in phase space when falling into the groups. Based on the time since infall, they divide the projected phase-space diagram into five regions. These regions are chosen to maximize the proportion of galaxies that belong to a specific time since they fall into the groups.

Fig. 9 shows the positions of our satellites in $(R, |\Delta V|)$ projected phase space, where R refers to the projected group-centric radius and $|\Delta V|$ is the peculiar line-of-sight velocity of each satellite, determined as the absolute value of the difference between its line-of-sight velocity and the average line-of-sight velocity of all satellites in the same group. All the velocities here are derived from spectroscopic redshifts. In Fig. 9, the satellites and isolated galaxies are labelled by blue points and orange crosses. The projected group-centric radius for isolated galaxies refers to the projected distance to groups which are

closest to them. Fig. 9 shows that the isolated galaxies and satellites are located in different areas in phase space, with most of the satellites located inside the $|\Delta V|/\sigma \times R/R_{180} = 1.2$ profile (red dashed line in Fig. 9).

We also show the infall regions given by Rhee et al. (2017) in Fig. 9. We scale the phase-space plot in R_{180} with $R_{180} \sim 0.77$ R_{vir}, assuming a Navarro, Frenk, and White (NFW; Navarro, Frenk & White 1997) profile with concentration parameter $c = 4$. The dominant galaxy populations in regions A, B, D, and E are first infallers, recent infallers, intermediate infallers, and ancient infallers, respectively. Region C is a mixing area with each population taking similar fraction. They find the galaxies follow the path in order of A, B, C, D, and E, as galaxies settle into groups potentials.

We use the bound of region A (grey) to identify the infalling isolated galaxies in our sample and to extend our measurements to larger projected radii. Fig. 10 shows stellar mass as a function of normalized projected group-centric radius for all galaxies (centrals in groups, isolated galaxies, and satellites). Isolated galaxies within
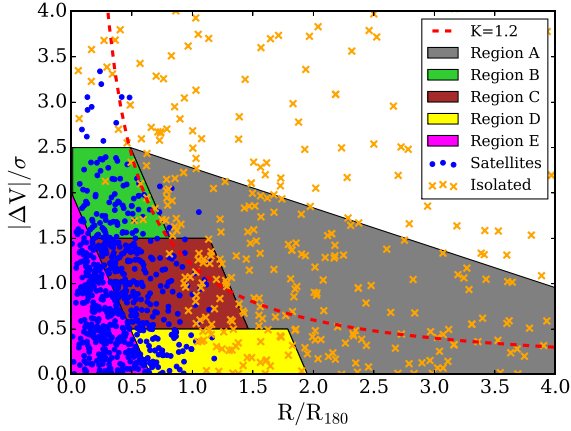
Figure 9. The phase-space diagram for the satellites (blue points) and isolated galaxies (orange crosses) in our sample. The red dashed line refers to the caustic profile with $K = 1.2$. The coloured five regions are given by Rhee et al. (2017), based on the time since infall.
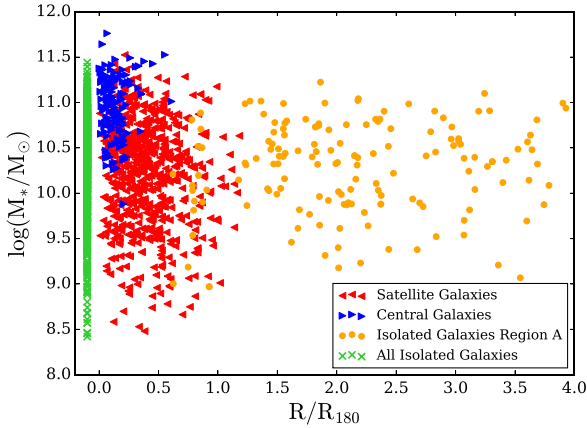

Figure 10. Stellar mass as a function of normalized projected group-centric radius for all galaxies in our sample. The centrals in groups, isolated galaxies, and satellites are marked with blue right triangles, green crosses, and red left triangles, respectively. Isolated galaxies are shifted from zero projected radius for clarity. The orange points are isolated galaxies located within Region A (see Fig. 9) of a neighbouring group, and the group-centric radius is the distance to their nearest neighbouring groups.

region A are included, with group-centric radius being the distance to the neighbouring group centre. In Fig. 10, we separately show all the isolated galaxies (not limited by the criterion above) in our sample at zero projected radius (the centre of their groups are themselves).

Now that we have a radial distance for each isolated galaxy close to a group, we stack them in bins of projected group-centric radius. As before, we only use galaxies in the range $10^{10.0} < M_* \leqslant 10^{11.5} \, \mathrm{M_\odot}$. The results in Fig. 11 and Table 4 show that isolated galaxies near neighbouring groups lack H I relative to isolated galaxies farther away from neighbouring groups. The H I gas fraction increases with normalized projected group-centric radius until $R \sim 2.0 \, R_{180}$. The sSFR also increases with the group-centric radius to $R \sim 2.0 \, R_{180}$. For comparison, we also reproduce here the H I properties and sSFR stacking results of satellite galaxies from Fig. 6, labelled as circle points. The H I properties and sSFR versus group centric radius relations for isolated galaxies can be well connected to those

for satellite galaxies. The increasing trend with radius for isolated galaxies seems to be the continuation of the trend for satellites. This suggests that H I gas loss starts well before a galaxy reaches R_{180} of a group and formally becomes a satellite.

For completeness, we also measured the H I content of galaxies as a function of local 3D density. We found that for centrals, satellites, and isolated galaxies, the H I mass decreases with increasing 3D density, which is consistent with the stacking results as a function of distance. This is because high local 3D densities always correspond to small group-centric radii.

The stacked mass spectra for isolated galaxies are shown in Appendix (Fig. A2).

5 DISCUSSION

Odekon et al. (2016) presented the H I content of galaxies measured by the 70 per cent complete ALFALFA survey and study the H I distribution in nearby groups and clusters. They compared the H I content in galaxies at fixed stellar mass and galaxy type in the centres of groups and clusters with the H I content in galaxies in control regions out to 4 Mpc surrounding each group or cluster. They found that at fixed stellar mass, the late-type galaxies in the centres of groups lack H I compared with galaxies in the outer control region. This is consistent with our results that at fixed stellar mass the satellites in the centres of groups lack H I relative to those at larger radii.

In Section 4.1, we compared our radial trends for low-mass and high-mass groups. Although the trend is more significant in high-mass groups, there is still an increase of H I mass with increasing distance from the group centre in low-mass groups with M_{halo} below $10^{13.5} \, h^{-1} \, \mathrm{M_\odot}$, well before galaxies reach the cluster environment. This is consistent with Odekon et al. (2016) and Brown et al. (2017), indicating existence of H I removal in isolated groups. The same conclusions are reached if we bin galaxies by projected densities, instead of group halo mass. However, for low densities the decrease of H I content in the centre of groups practically disappears.

In order to find the best predictors of galaxy properties, Odekon et al. (2016) ran regressions against six environment variables (group-centric radius r, normalized group-centric radius r/R_{200}, density Σ, group mass M_{200}, halo mass in the Yang catalogue, and central/satellite status in the Yang catalogue). By comparing the standardized slopes from regressions for log stellar mass, $g - i$ colour, log H I mass, and H I deficiency for blue cloud galaxies as a function of six different environment variables, they found that local density is the most effective predictor, while r/R_{200} and group-centric radius r are similarly less effective, followed by group size and halo mass. However, the opposite conclusion was reached by Brown et al. (2017), who stacked the H I spectra of 10 600 satellite galaxies measured by the ALFALFA survey to investigate environment-driven gas depletion in satellite galaxies. Brown et al. (2017) showed that gas content is depleted with increasing fixed aperture and nearest neighbour densities, but that halo mass is the most dominant environmental driver of H I removal in satellites. Specifically, when one fixes density and alters the halo mass, differences are larger than when density is changed at fixed halo mass. Besides, it is shown that at fixed sSFR gas fraction decreases more significantly with halo mass than with density. The conflicting results of which one of local density and halo mass can more effectively drive environmental H I removal are most likely due to different sample selection. Odekon et al. (2016) worked only with ALFALFA detections, while Brown et al. (2017) used staking. So, Odekon et al. (2016) focused on gas-rich galaxies for which the environment has just started affecting
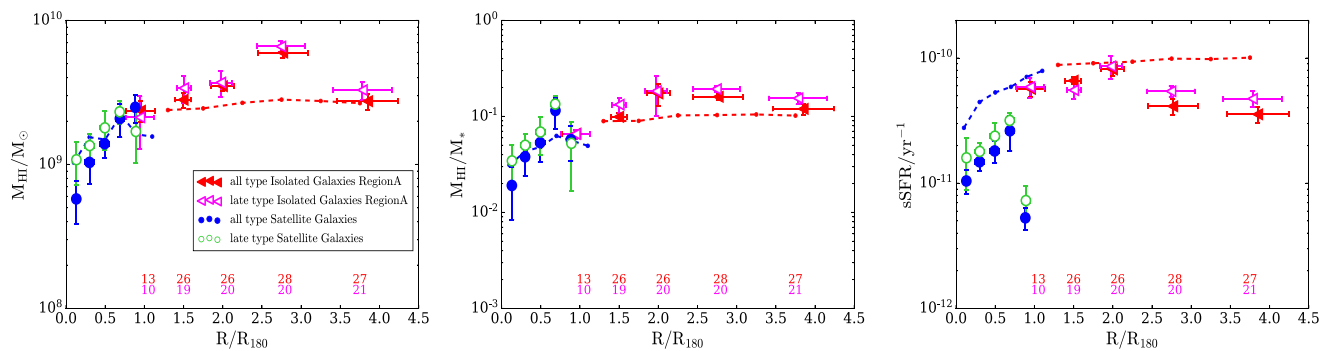
Figure 11. Same as Fig. 6, but for satellite galaxies (circle points; see Fig. 6) and infalling isolated galaxies (left-pointing triangles) in the range $10^{10.0} < M_* \leqslant 10^{11.5}$ $M_\odot$ as a function of normalized projected group-centric radius, extended out to greater radii. The results from the all-type and the late-type galaxies are labelled as filled and open points, respectively. For the isolated galaxies, the group-centric radius corresponds to the distance from the galaxy to the centre of its nearest group. The corresponding values are presented in Table 4 and Table 1. Each panel also overplots the measurement from SHARK simulation with red and blue dashed line corresponding to the all-type satellite galaxies and infalling isolated galaxies.

Table 4. Some basic statistics information and the stacking results of H I properties as a function of group-centric radius, for the all-type and the late-type isolated galaxies at $10^{10.0}$ $M_\odot < M_* \leq 10^{11.5}$ $M_\odot$, extended to larger radii. We illustrate the results in Fig. 11.

Radial bins (R_{180})	Radius (R_{180})	Number of galaxies	r_{50}/r_{90}	$\langle M_* \rangle$ (10^{10} h_{70}^{-2} $M_\odot$)	$\langle M_{\rm H\,I} \rangle$ (10^9 h_{70}^{-2} $M_\odot$)	$\langle M_{\rm H\,I}/M_* \rangle$	$\langle$ sSFR $\rangle$ ($10^{-11}/{\rm yr}^{-1}$)
All-type isolated galaxies							
(0.75,1.25]	1.04 ± 0.14	13	0.41 ± 0.06	4.1 ± 0.3	2.3 ± 0.5	0.07 ± 0.01	5.7 ± 0.9
(1.25,1.75]	1.50 ± 0.12	26	0.39 ± 0.07	4.3 ± 0.2	2.8 ± 0.3	0.10 ± 0.01	6.6 ± 0.4
(1.75,2.25]	1.98 ± 0.15	26	0.39 ± 0.06	4.4 ± 0.4	3.5 ± 0.3	0.17 ± 0.04	8.1 ± 0.9
(2.25,3.25]	2.76 ± 0.32	28	0.38 ± 0.06	4.6 ± 0.3	6.0 ± 0.6	0.16 ± 0.01	4.1 ± 0.8
(3.25,4.45]	3.85 ± 0.39	27	0.38 ± 0.06	4.2 ± 0.3	2.8 ± 0.4	0.12 ± 0.02	3.6 ± 0.4
Late-type isolated galaxies							
(0.75,1.25]	1.04 ± 0.14	10	0.43 ± 0.03	3.1 ± 0.2	2.1 ± 0.3	0.06 ± 0.01	5.9 ± 1.0
(1.25,1.75]	1.50 ± 0.12	19	0.42 ± 0.05	3.6 ± 0.3	3.4 ± 0.9	0.13 ± 0.02	5.5 ± 0.5
(1.75,2.25]	1.98 ± 0.15	20	0.41 ± 0.05	3.6 ± 0.5	3.7 ± 0.8	0.18 ± 0.08	8.6 ± 1.6
(2.25,3.25]	2.76 ± 0.32	20	0.41 ± 0.04	3.9 ± 0.3	6.6 ± 0.5	0.19 ± 0.01	5.4 ± 0.7
(3.25,4.45]	3.85 ± 0.39	21	0.40 ± 0.05	3.6 ± 0.3	3.3 ± 0.4	0.15 ± 0.02	4.7 ± 0.7

their evolution, while Brown et al. (2017) covered the entire range of gas fraction.

Following what is done in Hu et al. (2020a), we compare our results with the prediction from the SHARK (Lagos et al. 2018) semi-analytical model. We construct a light-cone with an area of ∼6900 deg^2 and redshift range of $z = 0$–0.1, containing all the galaxies with $M_\star \geq 10^5$ $M_\odot$ (see Chauhan et al. 2019 for details on how light-cones are constructed). Using the SHARK light-cone and the method described in Section 3, we stack the H I mass, H I mass fraction, and sSFR from SHARK galaxies with stellar masses $10^{10.0} < M_*/M_\odot \leq 10^{11.5}$ and apparent r-band magnitude $M_r < 17.7$ mag. For the stacking of isolated galaxies in SHARK, we only use the infalling galaxies in Region A (see Section 4.2). The results are presented in Fig. 11 as dashed lines.

Overall, SHARK qualitatively matches the radial trends of satellite galaxies (red points and lines) for both H I mass and H I mass fraction, with the only potential difference being a milder decrease towards the centre of groups, compared to our observational results. This is not surprising, given that the model does not include stripping of the cold gas phase. Indeed, Hu et al. (2020a) already highlighted the limitation of SHARK in reproducing the properties of satellite galaxies.

However, the most striking difference between the model and our observations is in the sSFR radial trends, where SHARK produces sSFRs a factor of ∼2–3 systematically higher than what is measured using our sample. The origin of this difference is unclear. Potential candidates are too high molecular gas masses and/or star formation efficiencies, suggesting that the lack of implementation of cold gas stripping alone cannot fully explain the differences highlighted here, as well as those presented in Hu et al. (2020a).

Because of the limited size of our sample, we cannot firmly determine which quantity between local density and halo mass is more closely associated with environment driven gas depletion. From the evidence presented here, it is possible to take our analysis a step further and quantify the H I properties versus group-centric radius relations at fixed stellar mass as a function of halo mass and density, only when a large enough galaxy sample can be accessed. Next-generation Square Kilometre Array (SKA) precursor facilities such as the Australian SKA Pathfinder (ASKAP) (Johnston et al. 2008; Meyer 2009), MeerKAT (Holwerda, Blyth & Baker 2012), Five-hundred-meter Aperture Spherical radio Telescope (FAST) (Duffy et al. 2008; Nan et al. 2011; Hu et al. 2020b), and WSRT/Aperture Tile in Focus (APERTIF) (Oosterloo et al. 2009) will enable large-area surveys to significant depths. It will very soon be possible to extend our measurements to significantly larger samples, making it feasible to further quantify the contribution of different mechanisms to the H I content increasing trend on radius, and potentially extend this to higher redshift.

Nevertheless, our results clearly highlight how the effect of environment on the gas content of galaxies may start well before they enter into the satellite phase, suggesting a potential role of pre-processing in the evolution of group and cluster galaxies (see also the recent work by Castignani et al. 2021). While statistically significant, it is important to remember that the effect of pre-processing does not affect H I content more than a factor of ≤ 2, implying that when galaxies formally become satellites they are still gas normal. In other words, the environmental processes making galaxies H I deficient, and ultimately passive, appear to be generally confined in the inner parts of groups and more efficient at high halo masses and projected galaxy density.

6 SUMMARY

In this work, we utilize an interferometric spectral stacking technique to study the distribution of H I content of galaxies and show that the galaxies in the centres of groups lack H I at fixed stellar mass and morphology relative to satellites in the group outskirts.

The data come from a 351-h WSRT H I survey covering ~ 35 deg^2 of the SDSS sky. After cross-matching with Yang's group catalogue, 1793 galaxies with SDSS redshifts in the range $0.01 < z < 0.11$ are available for stacking. 120 isolated galaxies and 457 satellites with stellar masses $10^{10.0} < M_*/M_\odot \leq 10^{11.5}$ are used to quantify the atomic hydrogen content of galaxies as a function of group-centric radius.

We find that the H I content of satellites monotonically decreases getting closer to the centre of groups. A similar trend is found for the sSFR. We test the trends against two environment variables, namely halo mass and local density. This shows that, for both high-mass and low-mass groups, galaxies in the central regions have smaller H I content than those in the outer regions, with the trends being more evident in high-mass groups. For galaxies in high local density regions, the H I content increases with group-centric radius. However, no clear relation between H I content and radius is apparent for galaxies in regions of low local density. Excitingly, we show that these radial trends continue at distances larger than R_{180}, once isolated galaxies in the infalling regions of groups are included. This provides tantalizing evidence that gas removal may start well before the crossing of the virial radius in groups and clusters. We also measure these trends in the late-type subsample to quantify the influence of morphology on our findings, and obtain similar results.

We compare our measurements with the semi-analytical model SHARK and find that, although the model reproduces the general decrease of H I mass with decreasing group-centric radius, it still fails in reproducing both H I and sSFR properties of our sample simultaneously.

DATA AVAILABILITY

The radio data analysed in this work are from WSRT and first reported in Geréb et al. (2015). The derived data can be accessed by sending request to the corresponding authors of this paper. The corresponding optical catalogue is from SDSS (York et al. 2000) Data Release 7.

REFERENCES

Abazajian K. N. et al., 2009, ApJS, 182, 543
Balogh M. L., Morris S. L., Yee H. K. C., Carlberg R. G., Ellingson E., 1999, ApJ, 527, 54
Bamford S. P. et al., 2009, MNRAS, 393, 1324
Benson A. J., 2010, Phys. Rep., 495, 33
Blanton M. R., Moustakas J., 2009, ARA&A, 47, 159
Bluck A. F. L. et al., 2016, MNRAS, 462, 2559
Brown T. et al., 2017, MNRAS, 466, 1275
Castignani G. et al., 2021, preprint (arXiv:2101.04389)
Catinella B. et al., 2013, MNRAS, 436, 34
Catinella B. et al., 2018, MNRAS, 476, 875
Chauhan G., Lagos C. d. P., Obreschkow D., Power C., Oman K., Elahi P. J., 2019, MNRAS, 488, 5898
Cooper M. C. et al., 2010, MNRAS, 409, 337
Cortese L., Catinella B., Boissier S., Boselli A., Heinis S., 2011, MNRAS, 415, 1797
Cortese L., Catinella B., Smith R., 2021, PASA, 38, e035
Davies R. D., Lewis B. M., 1973, MNRAS, 165, 231
Davies L. J. M. et al., 2019, MNRAS, 483, 5444
Dressler A., 1984, ARA&A, 22, 185
Duffy A. R., Battye R. A., Davies R. D., Moss A., Wilkinson P. N., 2008, MNRAS, 383, 150
Fabello S., Kauffmann G., Catinella B., Li C., Giovanelli R., Haynes M. P., 2012, MNRAS, 427, 2841
Geréb K., Morganti R., Oosterloo T. A., Hoppmann L., Staveley-Smith L., 2015, A&A, 580, A43
Giovanelli R., Haynes M. P., 1985, ApJ, 292, 404
Giovanelli R. et al., 2005, AJ, 130, 2598
Gómez P. L. et al., 2003, ApJ, 584, 210
Haynes M. P., Giovanelli R., Chincarini G. L., 1984, ARA&A, 22, 445
Holwerda B. W., Blyth S.-L., Baker A. J., 2012, in Tuffs R. J., Popescu C. C., eds, Proc. IAU Symp. 284, The Spectral Energy Distribution of Galaxies - SED 2011. Kluwer, Dordrecht, p. 496
Hu W. et al., 2019, MNRAS, 489, 1619 (Paper I)
Hu W., Catinella B., Cortese L., Staveley-Smith L., Lagos C. d. P., Chauhan G., Oosterloo T., Chen X., 2020a, MNRAS, 493, 1587
Hu W., Wang X., Wu F., Wang Y., Zhang P., Chen X., 2020b, MNRAS, 493, 5854
Johnston S. et al., 2008, Exp. Astron., 22, 151
Kauffmann G. et al., 2003, MNRAS, 341, 33
Kauffmann G., White S. D. M., Heckman T. M., Ménard B., Brinchmann J., Charlot S., Tremonti C., Brinkmann J., 2004, MNRAS, 353, 713
Kennicutt R. C., Jr, 1983, AJ, 88, 483
Lagos C. d. P., Tobar R. J., Robotham A. S. G., Obreschkow D., Mitchell P. D., Power C., Elahi P. J., 2018, MNRAS, 481, 3573
Lewis I. et al., 2002, MNRAS, 334, 673
Li J., Obreschkow D., Lagos C., Cortese L., Welker C., Džudžar R., 2020, MNRAS, 493, 5024
Mahajan S., Mamon G. A., Raychaudhury S., 2011, MNRAS, 416, 2882
Martin A. M., Giovanelli R., Haynes M. P., Guzzo L., 2012, ApJ, 750, 38

Meyer M., 2009, in Heald G., Serra P., eds, Proc. Sci., Exploring the HI Universe with ASKAP. SISSA, Trieste, PoS#15

Meyer M. J., Zwaan M. A., Webster R. L., Brown M. J. I., Staveley-Smith L., 2007, ApJ, 654, 702

Nan R. et al., 2011, Int. J. Mod. Phys. D, 20, 989

Navarro J. F., Frenk C. S., White S. D. M., 1997, ApJ, 490, 493

Odekon M. C. et al., 2016, ApJ, 824, 110

Oman K. A., Hudson M. J., 2016, MNRAS, 463, 3083

Oman K. A., Hudson M. J., Behroozi P. S., 2013, MNRAS, 431, 2307

Oosterloo T., Verheijen M. A. W., van Cappellen W., Bakker L., Heald G., Ivashina M., 2009, Proc. Sci., Apertif - The Focal-plane Array System for the WSRT. SISSA, Trieste, PoS#70

Pasquali A., Smith R., Gallazzi A., De Lucia G., Zibetti S., Hirschmann M., Yi S. K., 2019, MNRAS, 484, 1702

Peng Y.-j. et al., 2010, ApJ, 721, 193

Peng Y.-j., Lilly S. J., Renzini A., Carollo M., 2012, ApJ, 757, 4

Poggianti B. M., Smail I., Dressler A., Couch W. J., Barger A. J., Butcher H., Ellis R. S., Oemler A., Jr, 1999, ApJ, 518, 576

Rhee J., Smith R., Choi H., Yi S. K., Jaffé Y., Candlish G., Sánchez-Jánssen R., 2017, ApJ, 843, 128

Sault R. J., Teuben P. J., Wright M. C. H., 1995, in Shaw R. A., Payne H. E., Hayes J. J. E., eds, ASP Conf. Ser. Vol. 77, Astronomical Data Analysis Software and Systems IV. Astron. Soc. Pac., San Francisco, p. 433

Schaefer A. L. et al., 2017, MNRAS, 464, 121

Shimasaku K. et al., 2001, AJ, 122, 1238

Solanes J. M., Manrique A., García-Gómez C., González-Casado G., Giovanelli R., Haynes M. P., 2001, ApJ, 548, 97

Stark D. V. et al., 2016, ApJ, 832, 126

Toribio M. C., Solanes J. M., Giovanelli R., Haynes M. P., Martin A. M., 2011, ApJ, 732, 93

Wang E. et al., 2018, ApJ, 860, 102

Warren M. S., Abazajian K., Holz D. E., Teodoro L., 2006, ApJ, 646, 881

Wetzel A. R., Tinker J. L., Conroy C., 2012, MNRAS, 424, 232

Yang X., Mo H. J., van den Bosch F. C., Pasquali A., Li C., Barden M., 2007, ApJ, 671, 153

Yang X., Mo H. J., van den Bosch F. C., 2009, ApJ, 693, 830

Yang X., Mo H. J., van den Bosch F. C., Zhang Y., Han J., 2012, ApJ, 752, 41

York D. G. et al., 2000, AJ, 120, 1579

APPENDIX A: STACKED SPECTRA

We show the stacked mass spectra for satellite and isolated galaxies in Figs A1 and A2. The red-dashed lines show the region over which we do the integration to compute the average H i mass. The spectra for the late-type and the all-type sample are labelled with green and blue, respectively. A larger number of radius bin corresponds to a larger projected radius. Most of stacks give clear detections. But for satellites, the stacks in the first radial bin give marginally detections.
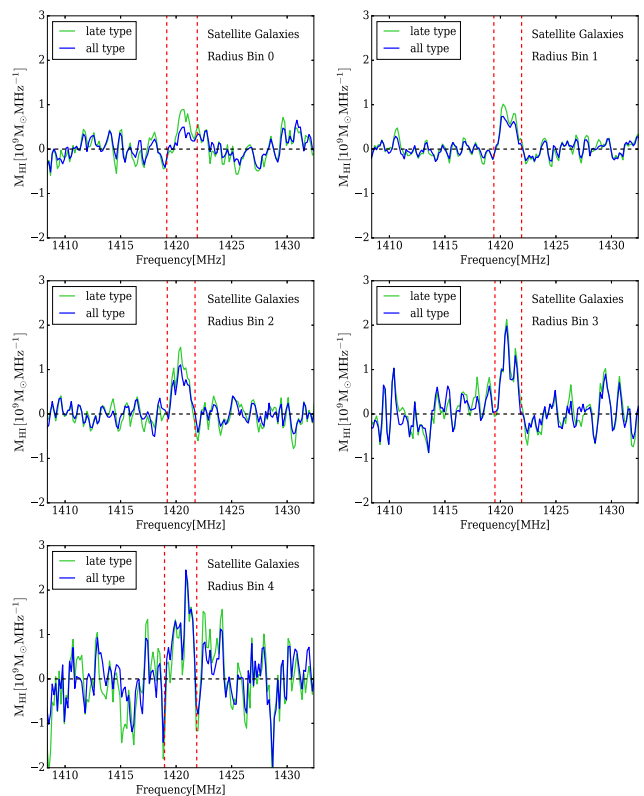

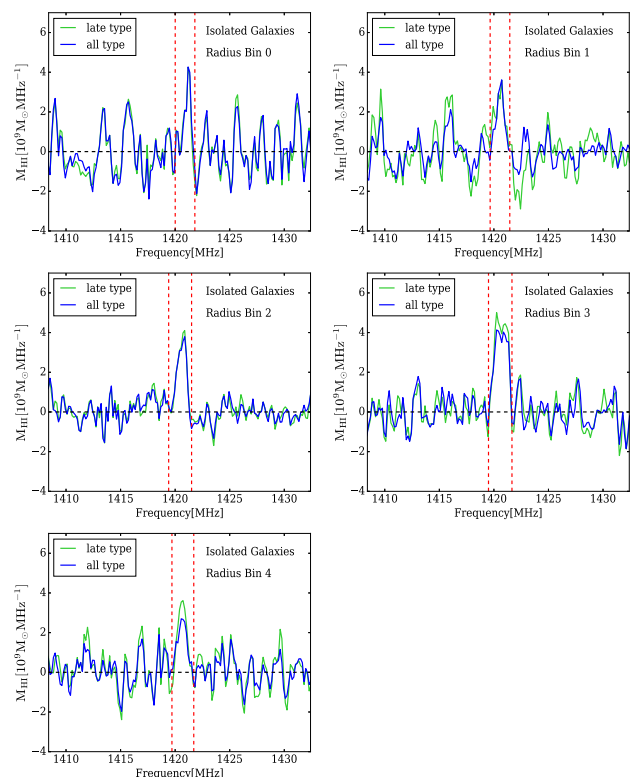**Figure A1.** The stacked mass spectra for satellite galaxies.

Figure A2. The stacked mass spectra for isolated galaxies.

This paper has been typeset from a TEX/LATEX file prepared by the author.